AIAA JOURNAL
Vol. 30, No. 10, October 1992

Flowfield of a Lifting Rotor in Hover: A Navier-Stokes Simulation

G. R. Srinivasan,* J. D. Baeder,† S. Obayashi,‡ and W. J. McCroskey§
NASA Ames Research Center, Moffett Field, California 94035

The viscous, three-dimensional flowfield of a helicopter rotor in hover is calculated by using an implicit, upwind, finite difference numerical method for the solution of thin-layer Navier-Stokes equations. The induced effects of the wake, including the interaction of tip vortices with successive blades, are calculated as a part of the overall flowfield solution without specifying any wake models. Comparison of the numerical results at subsonic and transonic flow conditions show good agreement with the experimental data for the surface pressures and the nearfield vortex trajectory. However, the captured vortex structure is diffused due to the coarse grids, but this appears to have minimal influence on the prediction of surface pressures. The paper also presents limited comparisons of the Navier-Stokes results with Euler results along with some discussion on grid refinement studies.

Introduction

THE accurate numerical simulation of the helicopter rotor flowfield in hover continues to be one of the most complex and challenging problems of applied aerodynamics. However, modern supercomputers and improved numerical algorithms have enabled advances to be made using computational fluid dynamics (CFD) to solve the equations of fluid motion for these complex flowfields. The solution schemes for these equations are usually coupled with integral wake models (e.g., vortex line elements, vortex lattices, or panels) to introduce the influence of the vortex wake. Techniques that implement this idea using a "prescribed" wake geometry encompass potential flow,[1-5] Euler,[6-8] and Navier-Stokes methods.[9-12] Also, a potential flow method[13] has been coupled with a "free" wake approach, in which the wake vorticity is specified, but is allowed to convect freely with the flow without constraining its trajectory. Other recent methods, including the present one, use direct techniques for the entire solution process, using Euler[14-17] and Navier-Stokes[18] flow solvers. In this context one can refer to these "free" wake methods as wake-capturing schemes, in analogy to shock capturing, whereas the "coupled" or "prescribed" wake methods are somewhat analogous to shock fitting. Finally, Navier-Stokes calculations have been performed[19] for the global time-averaged wake alone, with the details of the flow on the rotor itself prescribed.

The weakest link in the wake-coupled methodologies[1-12] is wake modeling. That is, the technique of specifying a prescribed wake has to be specialized for each blade shape, making it difficult to treat blade shapes with arbitrary twist, taper, and planforms. Therefore, the purpose of this study is to develop an improved calculation method for the solution of Navier-Stokes equations for the complete flowfield of a lifting rotor, including the wake and its induced effects. The vortex wake and its effects are captured as a part of the complete flowfield; thus, no arbitrary inputs or vortex-modeling approximations are necessary to describe the wake. In addition to the wake-capturing capabilities, the Navier-Stokes approach is chosen for the following reasons: 1) better tip-flow simulation, which involves resolving the flow separation and the formation of a concentrated tip vortex; 2) accurate simulation of strong viscous-inviscid interaction involving shock induced separation at high blade tip speeds and high collective pitch conditions; and 3) future modeling of retreating blade and dynamic stall regimes in forward flight.

The numerical code used in this study, called the transonic unsteady rotor Navier-Stokes (TURNS), is an improvement of the version that was developed previously in related studies with wake modeling.[9] A fundamental difference of this new numerical scheme is the use of Roe's upwinding in all three directions.[20] This feature, coupled with an implicit iterative procedure, has produced a fast, efficient, and accurate numerical scheme. In addition, a periodic boundary condition[17] has been implemented in the azimuthal direction, as described later in the text. These improvements allow the near wake to be computed well enough to approximately simulate the correct inflow through the rotor, thus obviating the need for the ad hoc wake modeling used previously.[9] These additional changes in the Navier-Stokes algorithm are based on some of the numerical procedures described in Ref. 21 and will be described briefly in the following sections.

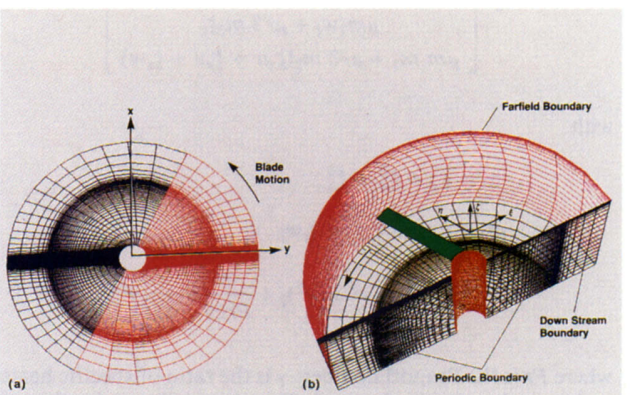

Fig. 1 A C-H cylindrical grid topology for a two-bladed rotor: a) view in the plane of the rotor, and b) isometric view showing the grid boundaries for a single blade.

Received Feb. 15, 1991; revision received March 31, 1992; accepted for publication April 7, 1992.

*Senior Staff Scientist, JAI Associates, Inc., Mountain View, CA. Associate Fellow AIAA.
†Research Scientist, U.S. Army Aeroflightdynamics Directorate. Member AIAA.
‡Senior Research Scientist, MCAT Institute, San Jose, CA. Senior Member AIAA.
§Senior Staff Scientist, U.S. Army Aeroflightdynamics Directorate. Fellow AIAA.

Governing Equations

The governing differential equations are the thin layer Navier-Stokes equations. These can be written in conservation law form in a generalized body-conforming curvilinear coordinate system as follows[22]:

$$\partial_\tau \hat{Q} + \partial_\xi \hat{E} + \partial_\eta \hat{F} + \partial_\zeta \hat{G} = \frac{\epsilon}{Re}\partial_\zeta \hat{S} + \hat{\mathfrak{R}} \tag{1}$$

where Re is the Reynolds number, $\epsilon = 0$ or 1 for the Euler or the Navier-Stokes equations, respectively, and $\tau = t$, $\xi = \xi(x, y, z, t)$, $\eta = \eta(x, y, z, t)$ and $\zeta = \zeta(x, y, z, t)$. The coordinate system (x, y, z, t) is attached to the blade (see Fig. 1). The vector of conserved quantities $\hat{Q}$ and the inviscid flux vectors $\hat{E}$, $\hat{F}$, and $\hat{G}$ are given by

$$\hat{Q} = \frac{1}{J}\begin{bmatrix} \rho \\ \rho u \\ \rho v \\ \rho w \\ e \end{bmatrix}, \qquad \hat{E} = \frac{1}{J}\begin{bmatrix} \rho U \\ \rho u U + \xi_x p \\ \rho v U + \xi_y p \\ \rho w U + \xi_z p \\ U H - \xi_t p \end{bmatrix} \tag{2}$$

$$\hat{F} = \frac{1}{J}\begin{bmatrix} \rho V \\ \rho u V + \eta_x p \\ \rho v V + \eta_y p \\ \rho w V + \eta_z p \\ V H - \eta_t p \end{bmatrix}, \qquad \hat{G} = \frac{1}{J}\begin{bmatrix} \rho W \\ \rho u W + \zeta_x p \\ \rho v W + \zeta_y p \\ \rho w W + \zeta_z p \\ W H - \zeta_t p \end{bmatrix}$$

In these equations, $H = (e + p)$ and U, V, and W are the contravariant velocity components defined, for example, as $U = \xi_t + \xi_x u + \xi_y v + \xi_z w$. The Cartesian velocity components are given by u, v, and w in the x, y, and z directions, respectively. Also, the density, pressure, and total energy per unit volume are represented by ρ, p, and e, respectively. Whereas the velocity and length scales are nondimensionalized by the characteristic velocity and length scales, given by the ambient sound speed a_∞ and the rotor blade chord c, the pressure p, density ρ, and the energy e are nondimensionalized by the freestream reference values p_∞/γ, ρ_∞, and $\rho_\infty a_\infty^2$, respectively. The quantities ξ_x, ξ_y, ξ_z, ξ_t, etc., are the coordinate transformation metrics, and J is the Jacobian of the transformation. For the thin-layer approximation used here, the viscous flux vector $\hat{S}$ is given by

$$\hat{S} = \frac{1}{J}\begin{bmatrix} 0 \\ \mu m_1 u_\zeta + \mu/3\, m_2 \zeta_x \\ \mu m_1 v_\zeta + \mu/3\, m_2 \zeta_y \\ \mu m_1 w_\zeta + \mu/3\, m_2 \zeta_z \\ \mu m_1 m_3 + \mu/3\, m_2 (\zeta_x u + \zeta_y v + \zeta_z w) \end{bmatrix} \tag{3}$$

with

$$m_1 = \zeta_x^2 + \zeta_y^2 + \zeta_z^2$$

$$m_2 = \zeta_x u_\zeta + \zeta_y v_\zeta + \zeta_z w_\zeta$$

$$m_3 = \frac{1}{2}(u^2 + v^2 + w^2)_\zeta + \frac{1}{Pr(\gamma - 1)}(a^2)_\zeta$$

where Pr is the Prandtl number, γ is the ratio of specific heats, and a is the speed of sound. For the noninertial reference frame used in this study, source terms have to be included in Eq. (1) to account for the centrifugal acceleration of the rotating blade.[23] The term $\hat{\mathfrak{R}}$ represents this in Eq. (1) and is given for a rigid rotor rotating in the x-y plane by

$$\hat{\mathfrak{R}} = \frac{1}{J}\begin{bmatrix} 0 \\ \Omega \rho v \\ -\Omega \rho u \\ 0 \\ 0 \end{bmatrix} \tag{4}$$

where Ω is the angular velocity of the rotor. The fluid pressure p is related to the conserved flow quantities through the nondimensional equation of state for a perfect gas given by

$$p = (\gamma - 1)\left\{e - \frac{\rho}{2}(u^2 + v^2 + w^2)\right\} \tag{5}$$

For turbulent viscous flows the nondimensional viscosity coefficient μ in $\hat{S}$ is computed as the sum of $\mu_l + \mu_t$, where the laminar viscosity, μ_l, is estimated using Sutherland's law and the turbulent viscosity, μ_t, is evaluated using the Baldwin-Lomax algebraic eddy viscosity model.[24]

Numerical Algorithm

A finite difference, upwind numerical algorithm is developed for the helicopter rotor applications. In this algorithm the evaluation of the inviscid fluxes is based on an upwind-biased flux-difference scheme originally suggested by Roe[25] and later extended to three-dimensional flows by Vatsa et al.[20] The chief advantage of using upwinding is that it eliminates the addition of explicit numerical dissipation and has been demonstrated to produce less dissipative numerical solutions.[20] This feature, coupled with a fine grid description in the tip region, increases the accuracy of the wake simulation. The van Leer monotone upstream-centered scheme for the conservative laws (MUSCL) approach[26] is used to obtain the second- or third-order accuracy with flux limiters in order to be total variation diminishing (TVD). The Lower-Upper-Symmetric Gauss-Seidel (LU-SGS) scheme, suggested by Jameson and Yoon,[27,28] is used for the implicit operator.

The space-discretized form of the differential Eq. (1) at node (j, k, l) is

$$\partial_\tau \hat{Q} = -\frac{\hat{E}_{j+\frac{1}{2}} - \hat{E}_{j-\frac{1}{2}}}{\Delta\xi} - \frac{\hat{F}_{k+\frac{1}{2}} - \hat{F}_{k-\frac{1}{2}}}{\Delta\eta} - \frac{\hat{G}_{l+\frac{1}{2}} - \hat{G}_{l-\frac{1}{2}}}{\Delta\zeta} + \frac{\epsilon}{Re}\frac{\hat{S}_{l+\frac{1}{2}} - \hat{S}_{l-\frac{1}{2}}}{\Delta\zeta} + \hat{\mathfrak{R}}_{j,k,l} \tag{6}$$

where j, k, and l correspond to the ξ, η, and ζ coordinate directions, respectively.

The application of Roe's upwinding to the numerical flux of the inviscid terms results in the locally one-dimensional form and can be written, e.g., in the ξ direction, as

$$\hat{E}[Q_L, Q_R, (\nabla\xi/J)_{j+\frac{1}{2}}] = \tfrac{1}{2}\{\hat{E}[Q_R, (\nabla\xi/J)_{j+\frac{1}{2}}] + \hat{E}[Q_L, (\nabla\xi/J)_{j+\frac{1}{2}}] - |A[Q_L, Q_R, (\nabla\xi/J)_{j+\frac{1}{2}}]|(Q_R - Q_L)\} \tag{7}$$

where A is the Roe-averaged Jacobian matrix and Q_L and Q_R are the left and right state variables, respectively. The scheme degenerates to the first-order accuracy if $Q_L = Q_j$ and $Q_R = Q_{j+1}$, for example, at the grid boundaries. Higher-order schemes can be constructed from a one-parameter family of interpolations for the primitive variables ρ, u, v, w, and p. For example, the left and right state variables for p are

$$P_L = \left\{1 + \frac{\psi_j}{4}[(1 - \kappa)\nabla + (1 + \kappa)\Delta]\right\}p_j \tag{8a}$$

$$P_R = \left\{1 - \frac{\psi_{j+1}}{4}\left[(1+\kappa)\nabla + (1-\kappa)\Delta\right]\right\} p_{j+1} \tag{8b}$$

where ∇ and Δ are backward and forward difference operators, and κ is a parameter that controls the construction of higher-order differencing schemes. For example, $\kappa = \frac{1}{3}$ is used in the present method to construct the third-order scheme. The limiter ψ is calculated by using Koren's differentiable limiter[29] as

$$\psi_j = \frac{3\nabla p_j \Delta p_j + \epsilon}{2(\Delta p_j - \nabla p_j)^2 + 3\nabla p_j \Delta p_j + \epsilon} \tag{9}$$

where a small constant, typically $\epsilon = 10^{-6}$, is added to prevent the division by zero. Similar formulas are used for the other primitive variables. The viscous flux terms are discretized using standard second-order central differencing.[22]

The time-marching integration procedure uses the LU-SGS method. The details of this scheme are described elsewhere.[21] Briefly, the LU-SGS method is a direct modification of the approximate lower-diagonal-upper (LDU) factorization to the unfactored implicit matrix. The resulting factorization can be regarded as the symmetric Gauss-Seidel relaxation method. The LDU factorization yields better stability than the simple LU factorization since the diagonal elements always have the absolute value of the Jacobian matrices.

The final form of this algorithm can be written for a first-order time-accurate scheme as

$$LDU\Delta\hat{Q}^n = -\Delta t RHS^n \tag{10}$$

where

$$L = I - \Delta t\hat{A}^-|_{j,k,l} + \Delta t\nabla_\xi\hat{A}^+ - \Delta t\hat{B}^-|_{j,k,l} + \Delta t\nabla_\eta\hat{B}^+ - \Delta t\hat{C}^-|_{j,k,l} + \Delta t\nabla_\zeta\hat{C}^+ \tag{11a}$$

$$D = [I + \Delta t(\hat{A}^+ - \hat{A}^- + \hat{B}^+ - \hat{B}^- + \hat{C}^+ - \hat{C}^-)|_{j,k,l}]^{-1} \tag{11b}$$

$$U = I + \Delta t\hat{A}^+|_{j,k,l} + \Delta t\Delta_\xi\hat{A}^- + \Delta t\hat{B}^+|_{j,k,l} + \Delta t\Delta_\eta\hat{B}^- + \Delta t\hat{C}^+|_{j,k,l} + \Delta t\Delta_\zeta\hat{C}^- + \frac{\partial R}{\partial Q} \tag{11c}$$

where Δt is the time step, RHS represents the discretized steady-state terms [e.g., Eq. (6)], and n refers to the current time level. Also, $A^+ = \frac{1}{2}(A + \sigma_\xi)$, $A^- = \frac{1}{2}(A - \sigma_\xi)$, $\sigma_\xi = (|U| + ar_\xi)(1+\epsilon)$, $\epsilon = 0.01$ typically, and $r_\xi = \sqrt{\xi_x^2 + \xi_y^2 + \xi_z^2}$. Also, in addition to the source term $\mathcal{R}$ added to the right-hand side of the Eq. (6), a source term Jacobian, $\partial R/\partial Q$, is added to either L or U operator on the left-hand side of Eq. (10). In the present case this is added to the U operator, as shown in Eq. (11c), and is given by

$$\frac{\partial R}{\partial Q} = \frac{1}{J}\begin{bmatrix} 0 & 0 & 0 & 0 & 0 \\ 0 & 0 & \Omega & 0 & 0 \\ 0 & -\Omega & 0 & 0 & 0 \\ 0 & 0 & 0 & 0 & 0 \\ 0 & 0 & 0 & 0 & 0 \end{bmatrix} \tag{12}$$

As a result of the simplified form of the Jacobian terms (e.g., $\hat{A}^+$), all of the diagonal elements of L, D, and U reduce to scalar elements. Thus, this method requires only two (one forward and one backward) sweeps with scalar inversions and leads to less factorization error. The source term adds two off-diagonal elements, resulting in slightly more computational work.

The present numerical scheme uses a modified finite-volume method for calculating the metrics. The chief advantage of standard finite-volume formulations is that both space and time metrics can be formed accurately[23] and that the freestream is captured accurately.[17] To be compatible with the present finite difference numerical scheme, the space metrics are evaluated here at the grid nodes instead of cell interfaces. However, the time metrics are evaluated in the same manner as in a finite difference scheme, which is computationally less expensive than a rigorous finite-volume calculation. As a result, freestream subtraction of the time-metric terms is then required to restore time accuracy.

In the calculation procedure the rotor blade is started from rest in a quiescent fluid and the evolution of the flowfield is monitored as the blade moves in azimuth. To take advantage of the quasisteady nature of the asymptotic hovering rotor flowfield in blade-fixed coordinates, a locally varying time step is used in the integration procedure to accelerate convergence, as suggested in Ref. 30.

Grids and Boundary Conditions

Body-conforming, single-block, three-dimensional computational grids were constructed for the rectangular rotor blades[31] by stacking and bending two-dimensional C-H grids which were generated by an elliptic solver.[32] Because of the cylindrical nature of the flow of a hovering rotor, a C-H cylindrical grid topology was chosen, as in Ref. 17, with the wraparound C direction in the chordwise direction and H type in the spanwise direction. In contrast to the experimental model rotor that has a square tip, the present grid generator approximates this as a bevel tip because of the H topology in the spanwise direction (see Ref. 33).

The standard viscous grids used here had 217 grid points in the wraparound (along the chord) direction, with 144 points on the body, 71 points in the spanwise (radial) direction with 55 points on the blade surface, and 61 points in the normal direction. The grid was clustered near the leading and trailing edges and near the tip region to resolve the tip vortex. It was also clustered in the normal direction to resolve the viscous flow near the blade surface. There are about 15 points in the boundary layer, with a spacing of the first grid point from the surface equal to 5×10^{-5} chord [$y^+ = \mathcal{O}(1)$]. A coarse grid was constructed from this fine viscous grid by removing every other point in all three directions. The inboard plane near the axis of rotation was located at a radial station equal to one chord. The grid outer boundaries were set at 8 chords in all directions. The same grids were used for the Euler calculations also.

Figure 1 shows the coarse grid that was used in the computations. Because of the symmetry of the hovering flow and the periodic boundary condition to be described, the calculations could be performed for only one blade. Figure 1a shows the cylindrical nature of the grid in the plane of the rotor, and Fig. 1b shows an isometric view of the grid boundary for a single blade. For clarity, the figure shows only the blade, side and bottom boundaries. Also shown is the coordinate system, where x is in the chordwise direction, y is in the radial direction, and z is in the normal direction. The blade motion is counterclockwise.

All the boundary conditions are applied explicitly. At the wall a no-slip boundary condition is used for the viscous calculations. The Euler calculations use an extrapolation of the contravariant velocities at the surface. The density at the wall is determined by a zero-order extrapolation. The pressure along the body surface is calculated from the normal momentum relation (see, e.g., Ref. 22). The total enery is then determined from the equation of state. To ensure continuity across the wake cut and also outboard of the blade tip, where the grid collapses to a singular plane because of H-grid topology, the

flow quantities are determined by averaging the flow variables from both sides of the singular plane.

To capture the information in the wake region of the blade, a periodicity condition is used in the blade azimuthal direction that swaps the flow information, after interpolation, at the front and back boundaries of the cylindrical grid (see Fig. 1b). This is also done in an explicit manner. The radial inboard and far-field boundaries, as well as the upper boundary of the cylindrical mesh, are updated by means of a characteristic-type boundary condition procedure, although Roe's upwinding used in the numerical procedure would otherwise treat the boundaries in a one-dimensional characteristic sense anyway. At the bottom boundary, the scene of the far-field wake, an approximate condition based on the normal velocity is used. For an outflow condition all conserved flow quantities are extrapolated from the grid interior, except for the energy, which is calculated by prescribing the freestream pressure.

Although the helicopter rotor operates in a quiescent fluid atmospere, unlike that in a fixed-wing airplane, it induces significant velocities at large distances from the rotor. Therefore, specification of no flow at the inflow boundaries of a computational box, which is typically small for economy, poses a difficulty for the prediction methods. This no-flow condition at the far-field boundaries produces a "closed box" environment for the rotor where the flow recirculates within the computational "box." This problem, and the large time required for the initial transients to decay, was recognized by Kramer et al.[14,34] who used an approximate vortex-element solution to specify an initial codition that produced a flow through the far-field boundaries of the computational box.

A simpler and more economical alternative was introduced in Ref. 35 using the concepts of a three-dimensional point sink and simple momentum theory as a guide. With this approach, the application of the previously mentioned characteristic-type

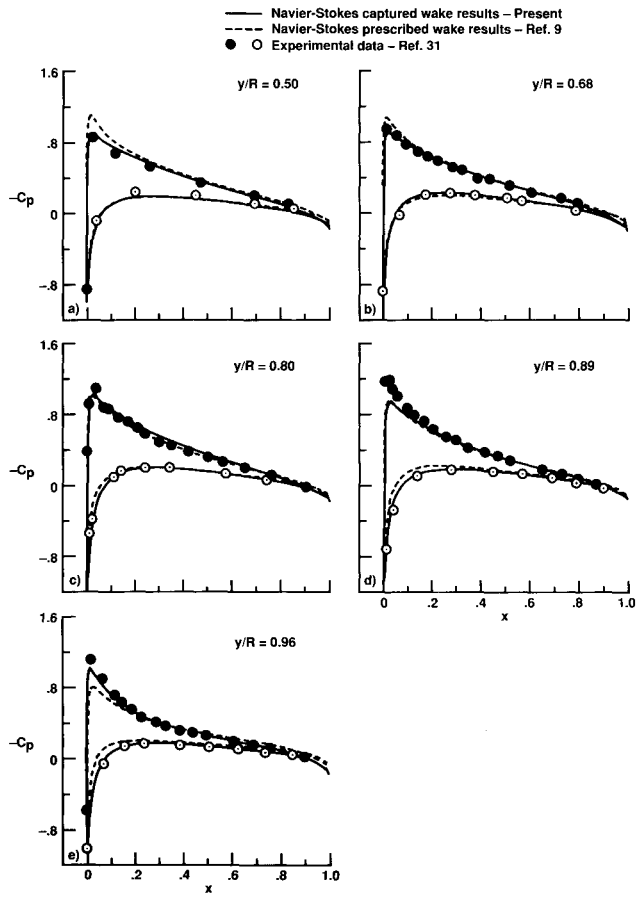

Fig. 2 Comparison of surface pressures for a lifting rotor in hover ($M_{tip} = 0.44$, $\theta_c = 8$ deg, and $Re = 1.92 \times 10^6$).

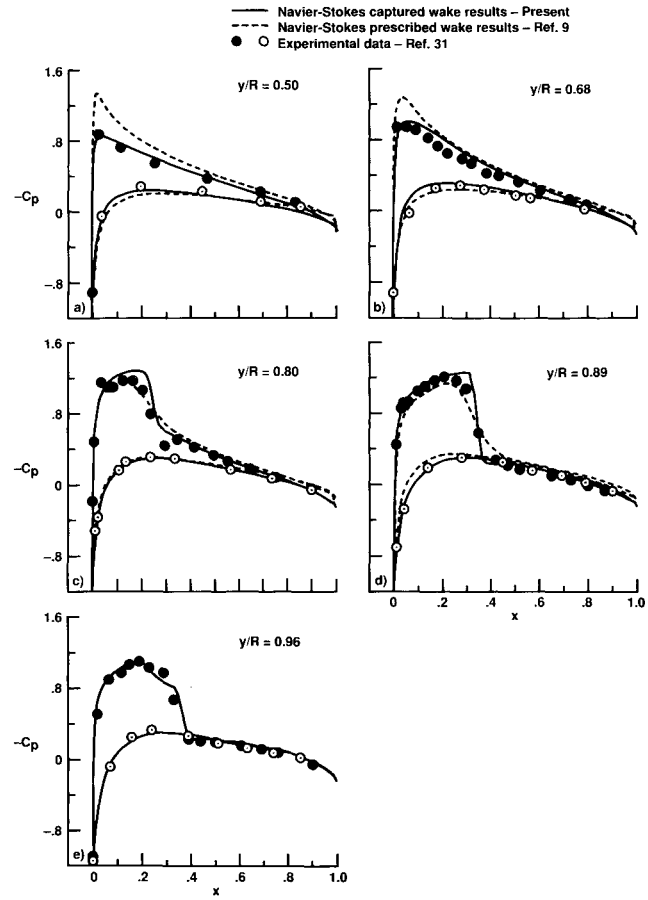

Fig. 3 Comparison of surface pressures for a lifting rotor in hover ($M_{tip} = 0.877$, $\theta_c = 8$ deg, and $Re = 3.93 \times 10^6$).

boundary condition produced a non-zero inflow at these boundaries. At the outflow boundary located at the far-field boundary below the rotor plane, the specification of the flow velocity is dictated from the momentum theory concepts, viz., the flow exit through a circular hole whose area is half that of the rotor disk, with an outflow velocity magnitude twice the momentum theory average value through the plane of the rotor. A characteristic-type numerical outflow boundary condition was applied across the exit plane by prescribing this outflow mass flux and extrapolating the other flow variables from within. With this, the flow smoothly entered and exited the computational box. Most of the results presented in this study used a "box-type" boundary conditions approach mentioned earlier. After recognizing the importance of smooth vortex wake descent below the rotor disk, one calculation was repeated with the new boundary conditions.

Results and Discussion

The test cases considered in this study correspond to the experimental model hover test conditions of Caradonna and Tung.[31] The experimental model consists of a two-bladed rigid rotor with rectangular planform blades with no twist or taper. The blades are made of NACA 0012 airfoil sections with an aspect ratio of 6. Three experimental conditions were chosen from the data: 1) tip Mach number $M_{tip} = 0.44$, collective pitch $\theta_c = 8$ deg, and the Reynolds number based on the blade tip speed and chord, $Re = 1.92 \times 10^6$; 2) $M_{tip} = 0.877$, $\theta_c = 8$ deg, and $Re = 3.93 \times 10^6$; and 3) $M_{tip} = 0.794$, $\theta_c = 12$ deg, and $Re = 3.55 \times 10^6$.

Fine Grid Navier-Stokes Results

Surface pressures are shown in Figs. 2-4 for the three experimental conditions considered. These calculations were done on a fine grid consisting of nearly one million points. Figure 2

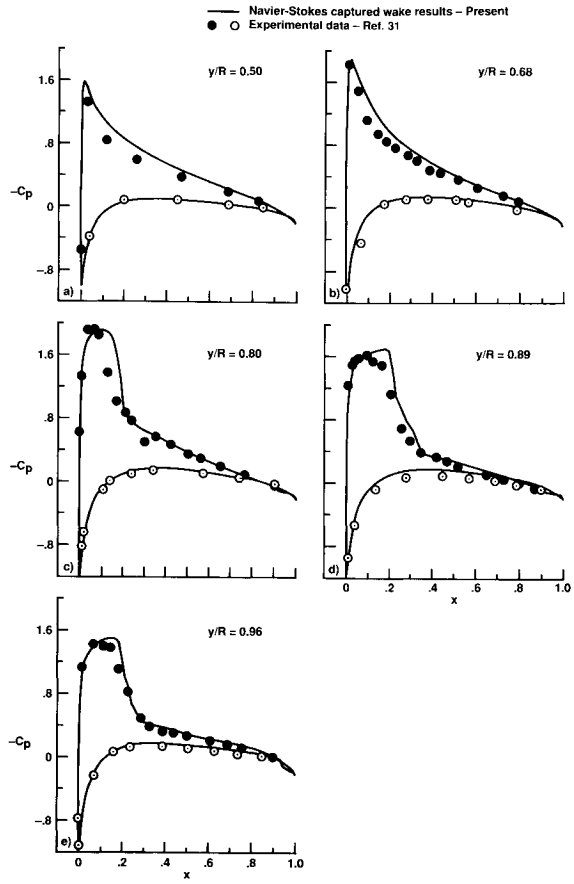

Fig. 4 Comparison of surface pressures for a lifting rotor in hover ($M_{tip} = 0.794$, $\theta_c = 12$ deg, and $Re = 3.55 \times 10^6$).

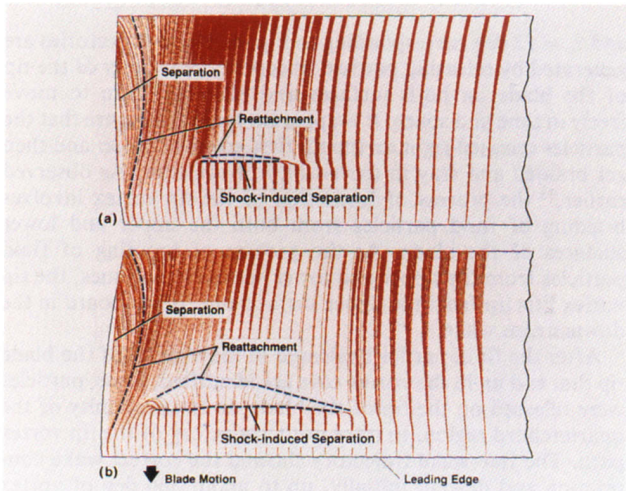

Fig. 5 Computed surface particle flow detail highlights the shock-induced boundary-layer separation for the flow conditions: a) $M_{tip} = 0.877$, $\theta_c = 8$ deg, and $Re = 3.93 \times 10^6$; and b) $M_{tip} = 0.794$, $\theta_c = 12$ deg, and $Re = 3.55 \times 10^6$.

shows the surface pressures for the conditions of $M_{tip} = 0.44$, $\theta_c = 8$ deg, and $Re = 1.92 \times 10^6$. In this figure the present calculations are compared with the experimental data of Ref. 31 and the results from a previous Navier-Stokes calculation that used a simple wake model (Ref. 9). The present calculations agree well with the experimental data for all radial stations. There are some improvements in the results at $y/R = 0.50$ and 0.96 over the previous results from Ref. 9. It should be pointed out that the calculations of Ref. 9 used a O-O grid topology with nearly 700,000 grid points having a grid clustering similar to the present grid.

Figure 3 shows a comparison of surface pressures for the condition of $M_{tip} = 0.877$, $\theta_c = 8$ deg, and $Re = 3.93 \times 10^6$. At this transonic flow condition, the present calculations show excellent agreement with the experimental data for all radial stations. In contrast to the calculations of Ref. 9, the present results show shock locations and shapes that are well captured due to the TVD upwinding used here. The inboard regions of the flow are also predicted more accurately; this indicates that the present computed wake is superior to the approximate wake model of Ref. 9.

Figure 4 shows a comparison of surface pressures for the condition of $M_{tip} = 0.794$, $\theta_c = 12$ deg, and $Re = 3.55 \times 10^6$. Because of the high collective pitch, this case is more severe in terms of the shock strength and shock-induced boundary-layer separation, even though the tip speed is slightly less than the previous case. The results show good agreement of the calculations with the experimental data, especially near the tip.

Figure 5 shows, through the surface particle flow, the extent of shock-induced boundary-layer separation for the transonic cases discussed earlier. These are created by releasing fluid particle tracers at one grid point above the surface and forcing them to stay in that plane. Figure 5a shows the details of this flow for the case of $M_{tip} = 0.877$ and $\theta_c = 8$ deg. The separation and reattachment locations are apparent in this figure. It is seen that this flow condition produces a mild shock-induced separation in the outboard part of the blade. In contrast, the shock-induced separation and viscous-inviscid interaction are much stronger for the case of $M_{tip} = 0.794$ and $\theta_c = 12$ deg. The surface particle flow pattern for this more severe case is shown in Fig. 5b. As seen, the extent of the separation is much larger for this flow condition than for the case of Fig. 5a. It is interesting, however, to note that the separation patterns in the tip region are approximately the same for these cases.

A general comparison of the present results with the experimental data can be made by examining the bound circulation distribution. Figure 6 shows such a plot of dimensionless circulation, $\Gamma/\Omega R^2$, as a function of r/R for $\theta_c = 8$ deg case and tip speeds of 0.44 and 0.877, corresponding to the data presented in Figs. 2 and 3. Here r is the radial distance from the rotation axis, R is the radius of the rotor, Ω is the constant angular velocity of the rotor, and Γ is the circulation, computed from the blade-element lift. Also shown are the integrated data from the experiments, which were reported to be essentially independent of tip speed. The calculations show a fair agreement with the experiments, except in the inboard

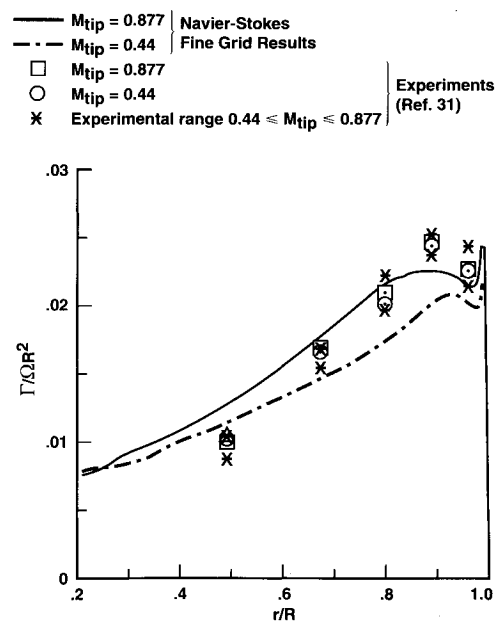

Fig. 6 Comparison of bound circulation distribution for the case of collective pitch $\theta_c = 8$ deg with tip speeds of $M_{tip} = 0.44$ and 0.877.

part of the blade. This suggests that only the near-field effects of the tip vortex are captured as well as desired. There are two possible reasons for the poor agreement in the inboard part of the blade: 1) The vortex wake becomes diffused in the far-field grid; hence, its induced effect is significantly diminished; and 2) the inboard plane boundary condition may be indequate. In contrast to the experimental observation of the bound cirulation distribution, the present calculations show some dependency on the blade tip speed.

In the tip region the agreement is also not very good. This may be due to the bevel tip that is used in the computations, compared to the square-tipped blade used in the experiments. However, overall, the surface pressure distributions give the appearance of agreeing better with the experiments than the bound-circulation distribution. Relatively minor discrepancies in the pressure distributions near the leading edge, where the experimental transducer locations are relatively sparse, seem to translate into significant differences in the circulation distribution.

The chief advantage of the Navier-Stokes methods is to predict the separated flow in the tip region and the associated detailed structure of the tip vortex. The prediction of the overall shed-wake geometry is the most important step in the process of accurately modeling the complete hover flowfield. The ability to preserve this shed wake (including the vortex structure) from numerical diffusion is a more complex issue. The path of the tip vortex is more important to the outboard blade loading, whereas the ability to convect this shed wake without significant numerical diffusion strongly influences the inflow in the inboard parts of the blade.

Figure 7 shows a near-field view of the tip vortex particle path trajectory for the experimental conditions of $M_{tip} = 0.794$ and $\theta_c = 12$ deg corresponding to Fig. 4. These trajectories are generated by releasing particle tracers in the vicinity of the tip of the blade on both surfaces and allowing them to move freely in time and space. It is apparent from this figure that the particles released right on the tip first group together and then get braided and stay in the vicinity of the core. As observed earlier,[33] the process of formation of the tip vortex involves braiding of fluid particles from both the upper and lower surfaces of the blade. As the process of braiding of fluid particles from the upper and lower surfaces continues, the tip vortex lifts up from the upper surface and rolls inboard in the downstream wake.

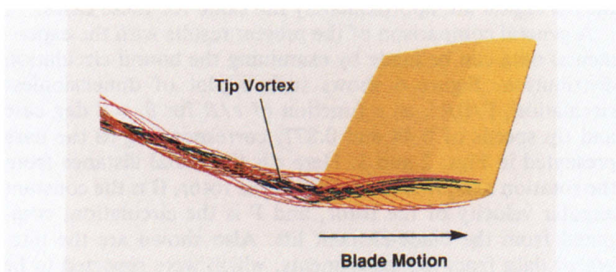

Fig. 7 Calculated tip vortex particle flow details showing the near-field view for the flow condition of $M_{tip} = 0.794$, $\theta_c = 12$ deg, and $Re = 3.55 \times 10^6$.

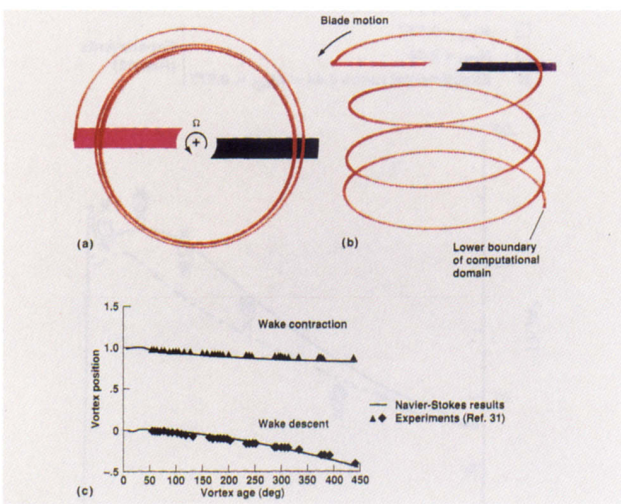

Fig. 8 Calculated tip vortex trajectory for the flow conditions of $M_{tip} = 0.44$, $\theta_c = 8$ deg, and $Re = 1.92 \times 10^6$: a) contraction of wake (looking from the top), b) captured tip vortex path and its vertical descent, and c) comparison of the calculated trajectory over 450 deg of vortex age with experiments.

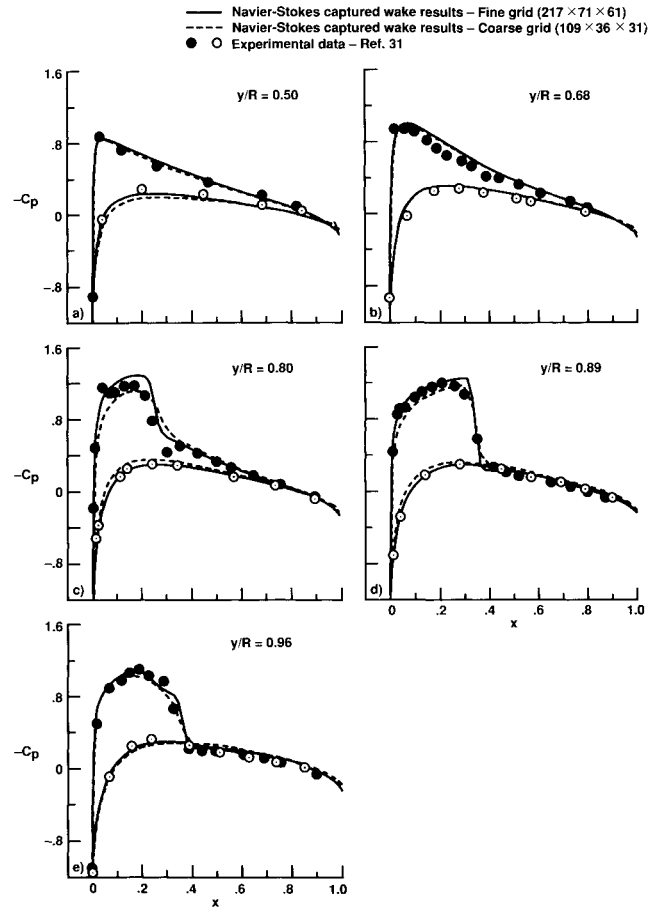

Fig. 9 Comparison of surface pressures with coarse and fine grids for the case of $M_{tip} = 0.877$, $\theta_c = 8$ deg, and $Re = 3.93 \times 10^6$.

After the fluid particles released in the vicinity of the blade tip that end up in the vortex core are identified, fewer particles were released on the tip of the blade, in the proximity of the quarterchord region, to trace out a trajectory of the tip vortex path. The free-wake trajectory showed the correct wake contraction and descent initially, up to about 360 deg of vortex age. Subsequently, the wake trajectory continued to descend, but it expanded in size and eventually ended up in the recirculating flow. This problem, due to the "box-type" far-field boundary condition used here, has been recently corrected by applying a point sink and simple momentum theory concepts,[35] as noted in the previous section. With this the flow smoothly enters the computational box and leaves through the exit boundary. The calculated vortex trajectory with this new boundary conditions is shown in Fig. 8. The wake contraction and descent trajectories are shown in Fig. 8a. Figure 8b shows a very good comparison of the calculated near-field trajectory with experiments.[31] Comparison of the calculated loads with the two methods of prescribing far-field boundary conditions showed only a 5% difference. However, the wake trajectory had the right characteristics of contraction and descent with the latter approach of specifying far-field boundary conditions.

Fine Grid vs Coarse Grid Results

The results presented in the preceeding sections were calculated on a fine grid of nearly one million points. The initial test calculations were made primarily on a coarse Navier-Stokes $109 \times 36 \times 31$ grid. This grid was generated by removing every other point from the fine grid in all three directions. The outer dimensions of the grid and the grid topology are thus the same as those for the previous fine grid.

Figure 9 shows a comparison of surface pressure distributions for the fine and coarse grids for the experimental condition of $M_{tip} = 0.877$, $\theta_c = 8$ deg, and $Re = 3.93 \times 10^6$. A general deterioration of the predicted surface pressure distributions can be seen for the coarse grids. In particular, the shocks are not as sharp as those for the fine grid. The inboard results, not shown here for $y/R < 0.5$, had much poorer comparison. The tip vortex structure is also very diffused due to the poor grid density in this region. However, typical converged solutions with this coarse grid took only about 1 h of CPU time on the Cray 2 supercomputer, down from about 15 h for the fine-grid cases.

Euler vs Navier-Stokes Results

As discussed earlier, there have been several attempts to capture rotor wakes using Euler methods.[14-17] The vortex formation in the tip region of a wing or a helicopter blade is a result of complex three-dimensional separated flow, and it is not clear how well the Euler methods are able to mimic viscous effects and separation to produce a vortex structure. Nevertheless, these Euler methods have been able to predict the pressure distributions and spanwise blade loading reasonably well for the outer part of the blade. Against this background, a limited comparison of surface pressures has been made of the Euler results with experiments and Navier-Stokes results.

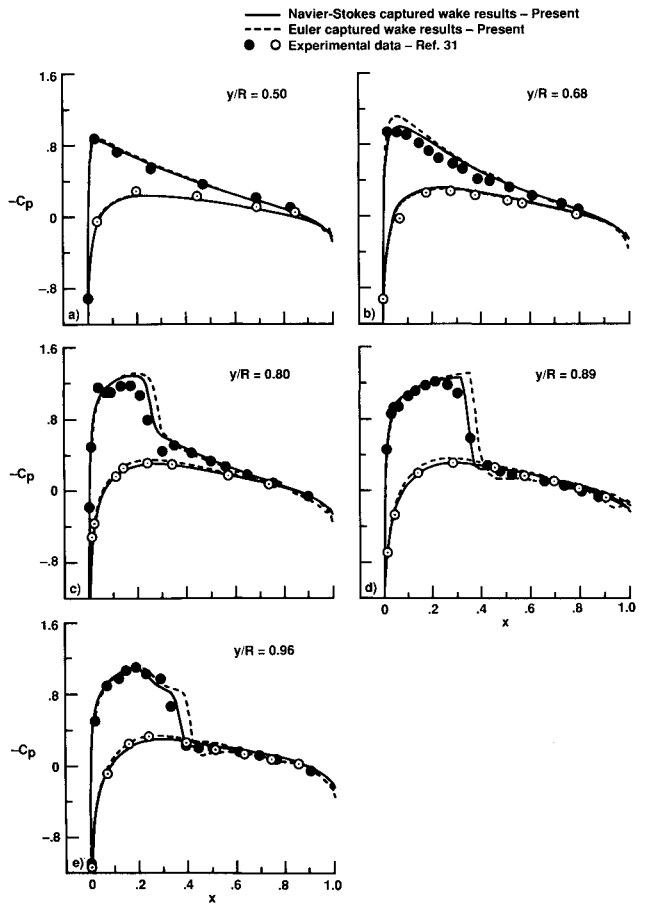

Fig. 10 Comparison of surface pressures for Euler and Navier-Stokes solutions; $M_{tip} = 0.877$, $\theta_c = 8$ deg, and $Re = 3.93 \times 10^6$.

The Euler calculations were made by turning off viscous terms in the TURNS code and using the same fine grid of about one million points used for viscous calculations. It should be noted that, even for this fine viscous grid, the Euler version of the code did not exhibit any stability problems.

A typical comparison of the Euler results with experiments[31] and the Navier-Stokes results is presented in Fig. 10 for the test conditions of $M_{tip} = 0.877$, $\theta_c = 8$ deg, and $Re = 3.93 \times 10^6$. Because it neglects viscous-inviscid interaction, the Euler method overpredicts the shock wave strength and position (for $y/R \geq 0.75$). Otherwise, the Euler results are in good agreement with the Navier-Stokes results, which show mild shock-induced separation for this flow condition (see Fig. 5a). The overall agreement of surface pressures certainly does not reflect the details of the flow near the blade surface, especially the separation pattern and vortex wake details as predicted by the Navier-Stokes method. A cursory examination of surface particle traces for Euler results showed that the flow is completely attached everywhere. Although it is not clear how the tip vortex is formed with flow separation only at the edges of the blade, the prediction of reasonably accurate surface pressures indicates that the induced inflow through the rotor is approximately correct and that the tip vortex *strength* was accurately captured. The recent Euler calculations of Strawn[36] indicate that the Euler methods capture the strength and peak velocities of the wing tip vortex as well as any Navier-Stokes method (e.g., see Ref. 33), which is still underpredicting peak velocities and tight braiding of the vortex. In current study, the details of the wake structure for the Euler results need to be investigated further.

Conclusions

The flowfield of a hovering rotor is calculated by means of an implicit, completely upwind, finite difference numerical procedure for the solution of thin-layer Navier-Stokes equations using a cylindrical C-H grid topology and body-fixed coordinates. The vortex wake and its induced effects are captured as a part of the overall numerical solution without specifying any wake structure or position, i.e., without any wake modeling. The use of periodic boundary conditions with a single blade enables the construction of a full helicopter rotor flowfield and thus saves computational time. The present numerical results are in good agreement with experimental data and represent an improvement over the previously published Navier-Stokes results that used a simple wake model. The method is thus very promising.

The good agreement of the surface pressures predicted by the Euler method with those of Navier-Stokes results seems to suggest that the details of surface flow, including separation and tip vortex details, are not important for predicting airloads. This needs further investigation. The robustness of the present methodology for Euler calculations is also demonstrated. Comparison of coarse and fine grid results indicates that the inboard ($y < 0.5$) air loads predicted with coarse grids had poor agreement with experiments and fine grid results, suggesting that the far-field wake effects are not as well captured with coarse grids. The numerical method is fairly efficient and runs at 145 MFLOPS on the Cray YMP supercomputer. The quasisteady Navier-Stokes calculations presented here for coarse and fine grids took ~ 1 h and 15 h of CPU time, respectively, on the Cray 2 supercomputer.

Acknowledgments

The first author would like to acknowledge the support of this research by the U.S. Army Research Office under Contracts DAAL03-88-C-0006 and DAAL03-90-C-0013. Computational time was provided by the Numerical Aerodynamics Simulation Facility and the Applied Computational Fluids Branch of NASA Ames Research Center.

References

[1]Caradonna, F. X., Desopper, A., and Tung, C., "Finite Difference Modeling of Rotor Flows Including Wake Effects," Paper 2.7,

Eighth European Rotorcraft Forum, Aix-en-Provence, France, Aug. 1982.

[2]Strawn, R. C., and Caradonna, F. X., "Conservative Full-Potential Model for Unsteady Transonic Rotor Flows," *AIAA Journal,* Vol. 25, No. 2, 1987, pp. 193–198.

[3]Strawn, R. C., and Tung, C., "The Prediction of Transonic Loading on Advancing Helicopter Rotors," NASA TM 88238, April 1986.

[4]Chang, I.-C., and Tung, C., "Numerical Solution of the Full-Potential Equation for Rotor and Oblique Wings Using a New Wake Model," AIAA Paper 85-0268, Jan. 1985.

[5]Egolf, T. A., and Sparks, S. P., "A Full Potential Flow Analysis with Realistic Wake Influence for Helicopter Rotor Airload Prediction," NASA Contractor Rept. 4007, Jan. 1987.

[6]Chang, I.-C., and Tung. C., "Euler Solution of the Transonic Flow for a Helicopter Rotor," AIAA Paper 87-0523, Jan. 1987.

[7]Agarwal, R. K., and Deese, J. E., "Euler Calculations for a Flowfield of a Helicopter Rotor in Hover," *Journal of Aircraft,* Vol. 24, No. 4, 1987, pp. 231–238.

[8]Sankar, N. L., Wake, B. E., and Lekoudis, S. G., "Solution of the Unsteady Euler Equations for Fixed and Rotor Wing Configurations," *Journal of Aircraft,* Vol. 23, No. 4, April 1986, pp. 283–289.

[9]Srinivasan, G. R., and McCroskey, W. J., "Navier-Stokes Calculations of Hovering Rotor Flowfields," *Journal of Aircraft,* Vol. 25, No. 10, 1988, pp. 865–874.

[10]Wake, B. E., and Sankar, N. L., "Solutions of the Navier-Stokes Equations for the Flow About a Rotor Blade," *Journal of the American Helicopter Society,* Vol. 34, No. 2, April 1989, pp. 13–23.

[11]Agarwal, R. K., and Deese, J. E., "Navier-Stokes Calculations of the Flowfield of a Helicopter Rotor in Hover," AIAA Paper 88-0106, Jan. 1988.

[12]Narramore, J. C., and Vermeland, R., "Use of Navier-Stokes Code to Predict Flow Phenomena Near Stall as Measured on a 0.658-Scale V-22 Tiltrotor Blade," AIAA Paper 89-1814, June 1989.

[13]Ramachandran, K., Tung. C., and Caradonna, F. X., "Rotor Hover Performance Prediction Using a Free-Wake, Computational Fluid Dynamics Method," *Journal of Aircraft,* Vol. 26, No. 12, 1989, pp. 1105–1110.

[14]Kramer, E., Hertel, J., and Wagner, S., "Computation of Subsonic and Transonic Helicopter Rotor Flow Using Euler Equations," *Vertica,* Vol. 12, No. 3, 1988, pp. 279–291.

[15]Kroll, N., "Computation of the Flow Fields of Propellers and Hovering Rotors Using Euler Equations," Paper No. 28, Twelfth European Rotorcraft Forum, Garmisch-Partenkirchen, Germany, Sept. 1986.

[16]Roberts, T. W., and Murman, E. M., "Solution Method for a Hovering Helicopter Rotor Using the Euler Equations," AIAA Paper 85-0436, Jan. 1985.

[17]Chen, C.-L., and McCroskey, W. J., "Numerical Simulation of Helicopter Multi-Bladed Rotor Flow," AIAA Paper 88-0046, Jan. 1988.

[18]Chen, C. S., Velkoff, H. R., and Tung, C., "Free-Wake Analysis of a Rotor in Hover," AIAA Paper 87-1245, June 1987.

[19]Rajagopalan, R. G., and Lim, C. K., "Laminar Flow Analysis of a Rotor in Hover," *Journal of the American Helicopter Society,* Vol. 36, No. 1, Jan. 1991, pp. 12–23.

[20]Vatsa, V. N., Thomas, J. L., and Wedan, B. W., "Navier-Stokes Computations of Prolate Spheroids at Angle of Attack," AIAA Paper 87-2627, Aug. 1987.

[21]Obayashi, S., "Numerical Simulation of Underexpanded Plumes Using Upwind Algorithms," AIAA Paper 88-4360-CP, Aug. 1988.

[22]Pulliam, T. H., and Steger, J. L., "Implicit Finite-Difference Simulations of Three-Dimensional Compressible Flow," *AIAA Journal,* Vol. 18, No. 2, 1980, pp. 159–167.

[23]Vinokur, M., "An Analysis of Finite-Difference and Finite-Volume Formulations of Conservation Laws," *Journal of Computational Physics,* Vol. 81, No. 1, March 1989, pp. 1–52.

[24]Baldwin, B. S., and Lomax, H., "Thin Layer Approximation and Algebraic Model for Separated Turbulent Flow," AIAA Paper 78-0257, Jan. 1978.

[25]Roe, P. L., "Approximate Riemann Solvers, Parameter Vectors, and Difference Schemes," *Journal of Computational Physics,* Vol. 43, No. 3, 1981, pp. 357–372.

[26]Anderson, W. K., Thomas, J. L., and van Leer, B., "A Comparison of Finite Volume Flux Vector Splittings for the Euler Equations," AIAA Paper 85-0122, Jan. 1985.

[27]Jameson, A., and Yoon, S., "Lower-Upper Implicit Schemes with Multiple Grids for the Euler Equations," *AIAA Journal,* Vol. 25, No. 7, 1987, pp. 929–935.

[28]Yoon, S., and Jameson, A., "An LU-SSOR Scheme for the Euler and Navier-Stokes Equations," AIAA Paper 87-0600, Jan. 1987.

[29]Koren, B., "Upwind Schemes, Multigrid and Defect Correction for the Steady Navier-Stokes Equations," *Proceedings of the 11th International Conference on Numerical Methods in Fluid Dynamics,* edited by D. L. Dwoyer, M. Y. Hussani, and R. G. Voigt, Springer-Verlag, Berlin, 1989.

[30]Srinivasan, G. R., Chyu, W. J., and Steger, J. L., "Computation of Simple Three-Dimensional Wing-Vortex Interaction in Transonic Flow," AIAA Paper 81-1206, June 1981.

[31]Caradonna, F. X., and Tung, C., "Experimental and Analytical Studies of a Model Helicopter Rotor in Hover," NASA TM 81232, Sept. 1981.

[32]Sorenson, R. L., "A Computer Program to Generate Two-Dimensional Grids About Airfoils and Other Shapes by the Use of Poisson's Equation," NASA TM 81198, May 1980.

[33]Srinivasan, G. R., McCroskey, W. J., Baeder, J. D., and Edwards, T. A., "Numerical Simulation of Tip Vortices of Wings in Subsonic and Transonic Flows," *AIAA Journal,* Vol. 26, No. 10, 1988, pp. 1153–1162.

[34]Hertel, J., Kramer, E., and Wagner, S., "Complete Euler Solution for a Rotor in Hover and a Propeller in Forward Flight," Paper I.4.2, Sixteenth European Rotorcraft Forum, Glasgow, Scotland, UK, Sept. 1990.

[35]Srinivasan, G. R., Raghavan, V., and Duque, E. P. N., "Flowfield Analysis of Modern Helicopter Rotors in Hover by Navier-Stokes Method," Proceedings of the American Helicopter Society-Royal Aeronautical Society International Technical Specialists Meeting on Rotorcraft Acoustics and Rotor Fluid Dynamics, Philadelphia, PA, Oct. 1991.

[36]Strawn, R. C., "Wing-Tip Vortex Calculations with an Unstructured Adaptive-Grid Euler Solver," *Proceedings of the 47th Annual Forum of the American Helicopter Society,* American Helicopter Society, Alexandria, VA, 1991, pp. 65–76.